J|A|C|S
ARTICLES

Published on Web 07/22/2010

Hollow V_2O_5 Nanoparticles (Fullerene-Like Analogues) Prepared by Laser Ablation

Roi Levi,[†] Maya Bar-Sadan,[‡] Ana Albu-Yaron,[†] Ronit Popovitz-Biro,[§]
Lothar Houben,[‡] Chen Shahar,[†] Andrey Enyashin,[⊥,||] Gotthard Seifert,[⊥]
Yehiam Prior,[¶] and Reshef Tenne*,[†]

Materials and Interfaces Department, Weizmann Institute of Science, Rehovot, Israel, Institute of Solid State Research and Ernst-Ruska Centre for Microscopy and Spectroscopy with Electrons, Research Centre Jülich GmbH, 52425 Jülich, Germany, Electron Microscopy Unit, Weizmann Institute of Science, PO Box 26, Rehovot 76100, Israel, Physikalische Chemie, Technische Universität Dresden, D-01062 Dresden, Germany, Institute of Solid State Chemistry, Ekaterinburg, Russia, Chemical Physics Department, Weizmann Institute of Science, PO Box 26, Rehovot 76100, Israel

Received May 1, 2010; E-mail: Reshef.Tenne@weizmann.ac.il

Abstract: Nanoparticles of materials with layered structure are able to spontaneously form closed-cage nanostructures such as nested fullerene-like nanoparticles and nanotubes. This propensity has been demonstrated in a large number of compounds such as WS_2, $NiCl_2$, and others. Layered metal oxides possess a higher ionic character and consequently are stiffer and cannot be evenly folded. Vanadium pentoxide (V_2O_5), a layered metal oxide, has received much attention due to its attractive qualities in numerous applications such as catalysis and electronic and optical devices and as an electrode material for lithium rechargeable batteries. The synthesis by pulsed laser ablation (PLA) of V_2O_5 hollow nanoparticles, which are closely (nearly) associated with inorganic "fullerene-like" (NIF-V_2O_5) nanoparticles, but not quite as perfect, is reported in the present work. The relation between the PLA conditions and the NIF-V_2O_5 morphology is elucidated. A new mechanism leading to hollow nanostructure via crystallization of lower density amorphous nanoparticles is proposed. Transmission electron microscopy (TEM) is used extensively in conjunction with structural modeling of the NIF-V_2O_5 in order to study the complex 3-D structure of the NIF-V_2O_5 nanoparticles. This structure was shown to be composed of facets with their low-energy surfaces pointing outward and seamed by defective domains. These understandings are used to formulate a formation mechanism and may improve the function of V_2O_5 in its many uses through additional morphological control. Furthermore, this study outlines which properties are required from layered compounds to fold into perfectly closed-cage IF nanoparticles.

---

1. Introduction

The properties of nanostructures are in many cases strongly size-dependent and may differ significantly from those of the bulk material.[1,2] Layered (two-dimensional [2-D]) materials, in general, have the ability to form closed-cage, hollow nanostructures, which may drastically differ in many of their properties from the bulk (platelet) morphology.[3] The stimulus for the formation of such closed-cage nanostructures lies in the energy gain obtained by seaming the otherwise dangling bonds of the numerous rim atoms. The gain in chemical energy compensates for the strain energy inherent to the distorted chemical bonds of the bended layers.[4]

Generally, folding along one axis of the nanoplatelets leads to inorganic nanotubes (INT). This does not require introduction of new topological elements into the nanostructure. However, folding along two axes is energetically more demanding and the strain can be alleviated by the insertion of either new topological elements or defects with the corresponding energy cost. For example, 12 pentagons are inserted into the hexagonal graphite layer to form carbon fullerenes, and 6 rhombi turn the hexagonal MoS_2 lattice into nanooctahedra.[5] It was suggested that these nanooctahedra are the smallest hollow cage structures of MoS_2,[5] i.e. the "true" MoS_2 fullerenes. In other cases, such as the closed-cage and nested nanoparticles of WS_2 and MoS_2,[1,3] point- and line-defects are often inserted into the molecular

---

[†] Materials and Interfaces Department, Weizmann Institute of Science.
[‡] Research Centre Jülich GmbH.
[§] Electron Microscopy Unit, Weizmann Institute of Science.
[⊥] Technische Universität Dresden.
[¶] Chemical Physics Department, Weizmann Institute of Science.
[||] Current address: Institute of Solid State Chemistry, Ural Branch of the Russian Academy of Science, 620219 Ekaterinburg, Russian Federation.

(1) Tenne, R.; Seifert, G. *Annu. Rev. Mater. Res.* **2009**, *39*, 387–413.
(2) Rao, C. N. R.; Achutharao, G. *Adv. Mater.* **2009**, *21*, 4208–4233.
(3) Tenne, R.; Margulis, L.; Genut, M.; Hodes, G. *Nature* **1992**, *360*, 444–446.
(4) Seifert, G.; Terrones, H.; Terrones, M.; Jungnickel, G.; Frauenheim, T. *Phys. Rev. Lett.* **2000**, *85*, 146–149.
(5) Enyashin, A. N.; Gemming, S.; Bar-Sadan, M.; Popovitz-Biro, R.; Hong, S. Y.; Prior, Y.; Tenne, R.; Seifert, G. *Angew. Chem., Int. Ed.* **2007**, *46*, 623–627.
(6) Popovitz-Biro, R.; Sallacan, N.; Tenne, R. *J. Mater. Chem.* **2003**, *13*, 1631–1634.

10.1021/ja103719x

layers in order to relieve the stress associated with the bending. These defects afford quasi-spherical nanoparticles, denoted as inorganic fullerene-like (IF). In fact, IF and INT nanoparticles are abundant among the metal dichalcogenides, dihalides, oxides, and other layered compounds.[1,2]

In contrast to graphite which is made of monatomic carbon sheets, inorganic layered compounds consist of a more complex 2-D network. Therefore, their folding into nanotubes (NT) and, particularly, fullerene-like structures is appreciably more demanding in terms of the elastic energy. Compounds with strong covalent character, such as MoS_2, are relatively flexible and can afford even bending of the layers. However, this is not the case in general for layered compounds with more ionic character, such as metal halides and oxides. Here, the hollow, closed-cage structures are found to be very faceted.[6]

Indeed, the synthesis of closed-cage nanoparticles (NP) from 2-D metal oxides, such as VO_x-nanotubes, often presents many challenges.[2] The 2-D layered structure in metal oxide compounds is usually very stiff due to their highly ionic character, which does not lend itself to facile shearing and folding of the layers.[7] The formation of a closed multiwall structure stipulates an increasing number of atoms in each layer. Preservation of the interlayer distance inevitably creates an incommensuration between the layers with regards to the original unit cell. A larger ionicity increases the effective charges on individual atoms and thus increases also the electrostatic forces between the layers. This in turn creates a resistance to interlayer shear as may be seen by the shear moduli or the C_{44} elastic constant. For example, the V_2O_5 C_{44} constant is 26 GPa,[8] while that of WS_2 is 2 GPa.[9]

Furthermore, formation of apex defects, which enable folding and closing of the layer into a hollow, closed cage (fullerene-like), cannot be easily achieved in materials with a complex unit cell such as (2-D) metal oxides. For example the number of atoms in the unit cell of V_2O_5 is 14 (as compared to 2 for carbon and 6 for MoS_2), which suggests a larger variety of possible structural combinations.

The synthetic obstacles are further compounded by the issue of stability. Metal oxides are sensitive to the surrounding conditions[10] as they are prone to reduction, e.g. by the electron beam, and tend to lose oxygen upon heating.[11] Additionally, water molecules from the humid ambient can be easily adsorbed to the polar metal−oxide bond.

Vanadium exists in multiple valence states, and thus vanadium and oxygen exhibit a rich phase diagram. Vanadium pentoxide (V_2O_5) possesses the maximal oxidation state among the large family of vanadium oxide compounds and is the most stable member of this series.[12] It is furthermore among the few metal oxides with versatile redox-dependent properties.[13] V_2O_5 is found in numerous applications such as catalysis,[14,15] ceramics,[16] solar cells,[17] chemical sensors,[18] a large variety of electrical and optical devices[19,20] and cathode material in rechargeable lithium batteries.[21] The multiple oxidation states of the vanadium oxides family entails facile reduction and oxidation chemistry which gives rise to potent catalysts.[14] The observed photo- and electrochromic behavior of V_2O_5 is exploited in information displays and color memory devices.[19] V_2O_5 has been extensively studied for use as functional ceramics.[16] Furthermore, rechargeable Li-intercalated V_2O_5 electrodes were investigated quite extensively due to their high-rate cyclability, high energy and power densities, as well as the abundance and low price of V_2O_5.[13]

V_2O_5 crystallizes in two different structures at room temperature. α-V_2O_5 (Figure 1a) is the prevalent structure. The γ polytype (Figure 1b) is obtained by deintercalation of Li^+ ions from γ-LiV_2O_5 bronze. It is metastable in ambient conditions and exhibits a sharp transition to α at 340 °C.[22] The V_2O_5 crystal becomes unstable upon heating in reducing or oxygen-deficient environments and tends to lose oxygen.[23] When liquid V_2O_5 (mp = 680 °C[24]) is quenched rapidly ($>10^6$ K·s^{-1}) amorphous V_2O_5 is formed.[25] A rapid crystallization of the amorphous material to α-V_2O_5 is observed at 200 °C.[25]

The α-V_2O_5 phase possesses an orthorhombic structure and is composed of alternating distorted VO_5 square pyramids which create double layers of O−V−O.[21] These layers are separated by a van der Waals (vdW) gap (the black arrow in Figure 1a). Thus, V_2O_5 shows strong anisotropic characteristics[21,26] typical to materials with layered (2-D) structure. The (010) plane (the basal or vdW plane) exhibits a lower surface energy as compared to that of the (100) and (001) planes. Note that, unlike the metal dichalcogenides where the vdW gap occurs along the $\underline{c}$ axis, the $\underline{b}$ axis is often used to define the vdW gap for metal oxides with layered structures. Due to the weak interlayer electrostatic binding force, the vdW gap (4.4 Å) provides a large number of intercalation sites. Intercalation of either lithium ions[27] or water[28] results in an expansion of the lattice parameters especially along the $\underline{b}$ axis (the vdW gap).

---

(7) Enyashin, A. N.; Gemming, S.; Seifert, G. In *Materials for Tomorrow*; Gemming, S., Schreiber, M., Suck, J.-B., Eds.; Springer-Verlag: Berlin, Heidelberg, 2007; Vol. 93, pp 33−57.

(8) Thomas, R.; Denis, M.; Jochen, M. S. *J. Phys.: Condens. Matter* **2009**, *21*, 145404.

(9) Kaplan-Ashiri, I.; Wagner, H. D.; Seifert, G.; Tenne, R. *Dekker Encyclopedia of Nanoscience and Nanotechnology*, 2nd ed.; 2009; pp 1617−1626.

(10) Albu-Yaron, A.; Arad, T.; Popovitz-Biro, R.; Bar-Sadan, M.; Prior, Y.; Jansen, M.; Tenne, R. *Angew. Chem., Int. Ed.* **2005**, *44*, 4169–4172.

(11) Singh, P.; Kaur, D. *J. Appl. Phys.* **2008**, *103*, 043507−9.

(12) Yan, B.; Liao, L.; You, Y. M.; Xu, X. J.; Zheng, Z.; Shen, Z. X.; Ma, J.; Tong, L. M.; Yu, T. *Adv. Mater.* **2009**, *21*, 2436–2440.

(13) Ng, S. H.; Patey, T. J.; Buechel, R.; Krumeich, F.; Wang, J. Z.; Liu, H. K.; Pratsinis, S. E.; Novak, P. *Phys. Chem. Chem. Phys.* **2009**, *11*, 3748–3755.

(14) Asim, N.; Radiman, S.; Yarmo, M. A.; Golriz, M. S. B. *Microporous Mesoporous Mater.* **2009**, *120*, 397–401.

(15) Penner, S.; Klotzer, B.; Jenewein, B. *Phys. Chem. Chem. Phys.* **2007**, *9*, 2428–2433.

(16) Zheng, C. M.; Zhang, X. M.; Qiao, Z. P.; Lei, D. M. *J. Solid State Chem.* **2001**, *159*, 181–185.

(17) Menezes, W. G.; Reis, D. M.; Benedetti, T. M.; Oliveira, M. M.; Soares, J. F.; Torresi, R. M.; Zarbin, A. J. G. *J. Colloid Interface Sci.* **2009**, *337*, 586–593.

(18) Ding, N.; Liu, S. H.; Chen, C. H.; Lieberwirth, I. *Appl. Phys. Lett.* **2008**, *93*, 1735101–3.

(19) Fang, G. J.; Liu, Z. L.; Wang, Y.; Liu, Y. H.; Yao, K. L. *J. Vac. Sci. Technol., A* **2001**, *19*, 887–892.

(20) Hu, Y.; Li, Z. C.; Zhang, Z. J.; Meng, D. Q. *Appl. Phys. Lett.* **2009**, *94*, 1031071–1031073.

(21) Beke, S.; Giorgio, S.; Korosi, L.; Nanai, L.; Marine, W. *Thin Solid Films* **2008**, *516*, 4659–4664.

(22) Cocciantelli, J. M.; Gravereau, P.; Doumerc, J. P.; Pouchard, M.; Hagenmuller, P. *J. Solid State Chem.* **1991**, *93*, 497–502.

(23) Benmoussa, M.; Ibnouelghazi, E.; Bennouna, A.; Ameziane, E. L. *Thin Solid Films* **1995**, *265*, 22–28.

(24) Ikemiya, N.; Umemoto, J.; Hara, S.; Ogino, K. *ISIJ Int.* **1993**, *33*, 156–165.

(25) Rivoalen, L.; Revcolevschi, A.; Livage, J.; Collongues, R. *J. Non-Cryst. Solids* **1976**, *21*, 171–179.

(26) Witko, M.; Hermann, K.; Tokarz, R. *Catal. Today* **1999**, *50*, 553–565.

(27) Wang, Y.; Takahashi, K.; Lee, K.; Cao, G. Z. *Adv. Funct. Mater.* **2006**, *16*, 1133–1144.

(28) Petkov, V.; Trikalitis, P. N.; Bozin, E. S.; Billinge, S. J. L.; Vogt, T.; Kanatzidis, M. G. *J. Am. Chem. Soc.* **2002**, *124*, 10157–10162.

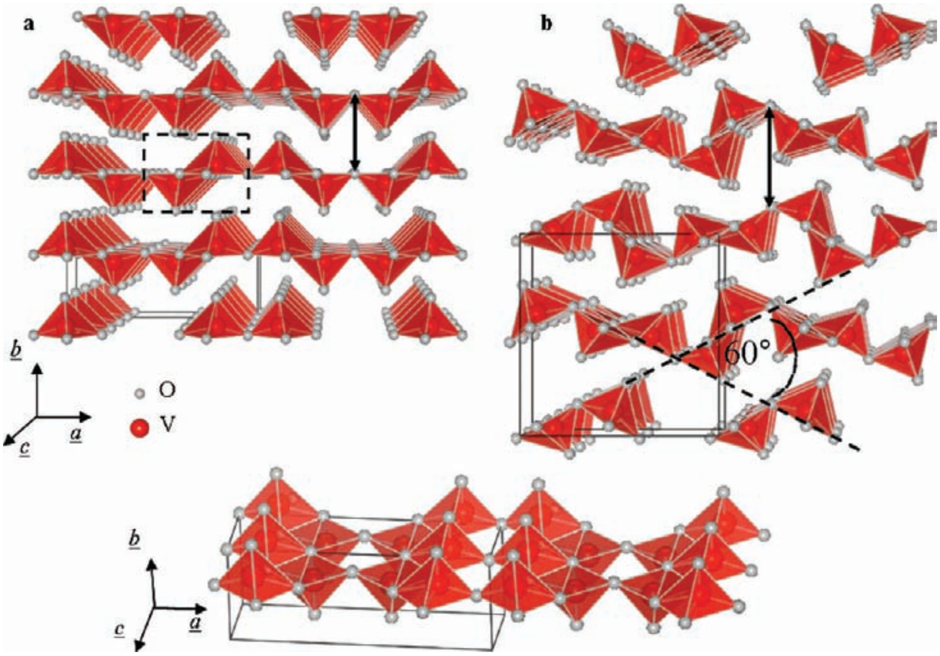

Figure 1. Perspective views of (a) α-V_2O_5.[22] (b) γ -V_2O_5 crystal structures[55] (the unit cell dimensions are $\underline{a} = 11.51$ Å, $\underline{b} = 4.37$ Å, and $\underline{c} = 3.56$ Å and $\underline{a} = 9.94$ Å, $\underline{b} = 10.04$ Å, $\underline{c} = 3.58$ Å, respectively). The dashed box marks the element twisted 180° as part of the transformation of the α-V_2O_5 unit cell to the γ -V_2O_5 unit cell. The black arrows mark the vdW gap. (c) Partial layer of α-V_2O_5 slightly tilted for clarity.

In contrast to many of the metal dichalcogenide and metal dihalide compounds which possess a fully symmetric structure in the basal plane ($\underline{a} = \underline{b}$), here the two lattice vectors in the plane ($\underline{a} \neq \underline{c}$) differ from each other. In order to tessellate the V_2O_5 rectangular patches into a polyhedral structure with low surface energy (0 1 0) faces, seaming of $\underline{a}$ (1 0 0) and $\underline{c}$ (0 0 1) edges becomes inevitable (*vide infra*). Unfortunately, the orthorhombic crystal structure does not lend itself to perfect seaming of perpendicular 2-D layers and leads to imperfections at the edges of the layers. Furthermore, the two opposing prismatic edges of the MoS_2 layer, i.e. the (1 1 0) and (1 −1 0) planes, are sulfur and molybdenum terminated, respectively. Hence, the seaming of the folded layer does not violate the electroneutrality of the (MoS_2) tube. This is not the case with V_2O_5 where the opposite edges are oxygen terminated. This means that seaming of the edges of the folded layers would require the unlikely formation of oxygen−oxygen bonds. Alternatively, loss of a row of oxygen atoms of one edge could establish a perfect seaming of the two edges in this case.

γ-V_2O_5 has a layered structure as well which resembles that of α-V_2O_5. As the basic element of both structures (marked in Figure 1a by the dashed box) remains the same, the γ-V_2O_5 unit cell may be obtained from that of α-V_2O_5 by a few rearrangements. Half of the VO_5 square pyramids in the α-V_2O_5 unit cell (marked in Figure 1a by the dashed box) are twisted by 180° with respect to the $\underline{a}$ axis. The layers then perform alternating turns of 60° with respect to the $\underline{c}$ axis (Figure 1b). While these twists give the γ-V_2O_5 layers a greater flexibility for bending, they also render the structure metastable.

A large variety of nanostructures of V_2O_5 have been synthesized. These include composite alkyl-amine-VO_x NT and nanoscrolls,[29] nanowires,[30] nanoribbons,[12,31] nanorods,[12,20,32−34] nanoneedles,[13,35] nanoplatelets,[35] and NP.[13,14,17,18,35,36] Microstructures such as hollow microspheres composed of nanorods[37] and microtubes[38] were reported as well. The composite alkyl-amine-VO_x nanotubes (VO_x-NT)[29] are of a particular interest for a number of reasons. The self-assembling alkyl-amine molecules attach to the V_2O_5 backbone, providing extra flexibility and allowing it to fold onto itself even under the mild temperatures (180 °C) used in the hydrothermal synthesis. While the VO_x-NT show great promise for variety of applications, the main obstacle is that the NT prepared show a large degree of disorder which hampers their mechanical as well as electrical behavior. Furthermore, attempts to remove the alkyl-amine molecules were only partially successful and ultimately lead to the destruction of the VO_x-NT.[29] While pure NT-V_2O_5 were the subject of quantum-mechanical calculations[39] no genuine V_2O_5 closed-cage nanostructures have been reported to date.

An equally large variety of chemical and physical methods has been utilized for the preparation of the V_2O_5 nanostructures. These include dry processes such as flame spray- and oxidative pyrolysis,[13,16] thermal treatment,[17,20] microwave plasma torch,[35] laser pyrolysis,[36] laser-assisted metal oxidation,[38] and wet processes such as the aforementioned templating methods,[14,32,34] chemical synthesis,[30] electrochemical deposition,[13,16] self-

---

(29) Spahr, M. E.; Bitterli, P.; Nesper, R.; Muller, M.; Krumeich, F.; Nissen, H. U. *Angew. Chem., Int. Ed.* **1998**, *37*, 1263–1265.

(30) Zhou, F.; Zhao, X. M.; Liu, Y. Q.; Yuan, C. G.; Li, L. *Eur. J. Inorg. Chem.* **2008**, 2506–2509.

(31) Chou, S. L.; Wang, J. Z.; Sun, J. Z.; Wexler, D.; Forsyth, M.; Liu, H. K.; MacFarlane, D. R.; Dou, S. X. *Chem. Mater.* **2008**, *20*, 7044–7051.

(32) Ajayan, P. M.; Stephan, O.; Redlich, P.; Colliex, C. *Nature* **1995**, *375*, 564–567.

(33) Pinna, N.; Wild, U.; Urban, J.; Schlogl, R. *Adv. Mater.* **2003**, *15*, 329–331.

(34) Satishkumar, B. C.; Govindaraj, A.; Nath, M.; Rao, C. N. R. *J. Mater. Chem.* **2000**, *10*, 2115–2119.

(35) Kim, J. H.; Hong, Y. C.; Uhm, H. S. *Surf. Coatings Technol.* **2007**, *201*, 5114–5120.

(36) Bi, X.; Gardner, J. T.; Kumar, S.; Kambe, N. NanoGram Corporation. U.S. Patent 5,589,514, 1999.

(37) Cao, A. M.; Hu, J. S.; Liang, H. P.; Wan, L. J. *Angew. Chem., Int. Ed.* **2005**, *44*, 4391–4395.

(38) Nanai, L.; George, T. F. *J. Mater. Res.* **1997**, *12*, 283–284.

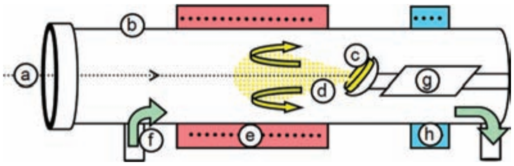

Figure 2. Laser ablation scheme. (a) Laser beam. (b) Quartz tube. (c) Solid V_2O_5 pellet. (d) Recoiling plume. (e) Furnace. (f) Oxygen carrier gas inlet. (g) Quartz collecting plate. (h) Liquid nitrogen cooling coil.

assembly,[37] and sol−gel synthesis.[40] Additionally, pulsed laser ablation (PLA) has been used extensively for deposition of textured (highly oriented) layers of V_2O_5[18−20] and for the synthesis of a variety of nanostructures.[21,41,42]

During PLA the laser beam hits a solid target and ablates it. The recoil from the laser beam creates a plume which may consist of plasma, vapors, liquid droplets, and solid particles.[43,44] This plume then undergoes a rapid quenching ($>10^9$ K·s^{-1}) due to the high temperature of the plume with respect to the ambient (∼2000 °C[41]). The violent and rapid nature of this process, which is far from equilibrium, leads to the formation of nanostructures with high internal energy.[42] Subsequent heating of the ablated plume was shown to provide effective relaxation (annealing) of the nanostructures to their respective lowest-energy configuration.[42]

The present work is dedicated to the synthesis of hollow and closed V_2O_5 nanoparticles (NIF-V_2O_5) with a structure analogous to that of IF, but having a structure which is not quite as perfectly crystalline. Extensive electron microscopy analysis is carried out in order to investigate the relation between the reaction conditions and the product morphology. The NIF-V_2O_5 structures are also studied through model considerations, which are further used in the elucidation of a formation mechanism. It is concluded that, due to their structural complexity and the large mechanical stiffness, these V_2O_5 nanostructures cannot be perfectly seamed into hollow, closed cages. Nonetheless, partial remediation for their extra energy in the nanoregime is gained by presenting hollow, patch-wise nanostructures with their van der Waals faces (0 1 0) pointing outward, i.e. with their ⟨0 1 0⟩ (<u>b</u>) direction perpendicular to the surface of the nanoparticle. It is furthermore shown that annealing of the plume at 340−500 °C leads to strong faceting of the nanoparticles, which is indicative of a further reduction in their internal energy.

2. Experimental Section

2.1. Laser Ablation. Pulsed laser ablation (PLA) of solid V_2O_5 pellets was performed with an Nd:YAG laser ($\lambda = 532$ nm, pulse width 8 ns, pulse repetition rate 10 Hz, ∼30 mJ/pulse) and O_2 carrier gas (flow rate of 100−200 cm^3·min^{-1}) at temperatures between 50 to 500 °C (Figure 2). A scheme of the system used for the PLA is described in Figure 2. The incident laser beam (a) passes through a quartz window into the quartz tube (b) and ablates the solid V_2O_5 pellet (c). The nanosecond laser pulse ablates the target and creates a plume (d) which is rapidly quenched and concomitantly recoils into the furnace (e) for a short annealing. The carrier gas (f) then deflects this plume by 180°, and the products are then deposited on a collection plate (g), which is cooled by a liquid nitrogen coil (h). During the deflection of the plume a short annealing takes place in the furnace (e) which controls the temperature of the process. Increasing the flow rate reduces the residence time of the products in the furnace, i.e. annealing time (3−6 s). The conditions were chosen according to V_2O_5 properties: melting point (680 °C[24]), oxygen loss due to heating, and the optical band gaps—indirect at 1.9 eV and direct at 2.3 eV.[45,46]

Considerable amounts of the products were found to condense on the quartz tube walls during the PLA. The total weight of products collected from the reactor ranged from 15 to 30 mg for a 30-min PLA experiment. In order to examine the products, various locations along the tube were sampled.

2.2. Transmission Electron Microscopy (TEM). The product on the collection plate was transferred to TEM grids. The grids were examined with TEM at various tilt angles (Philips, CM-120, 120 kV); high-resolution TEM (HRTEM; FEI Tecnai F-30, 300 kV) and aberration-corrected TEM (FEI Titan 80 kV). The products were further examined by SEM (LEO model Supra 55vp, acceleration voltage under 5 kV, working distance of 5−6 mm). Energy-dispersive spectrometry (EDS) was performed inside the TEM (Phoenix EDAX) as well as electron diffraction (ED).

2.3. Simulation of TEM Images. Simulated images of the closed-cage nanoparticles were calculated from supercell data containing the atomic coordinates of the structures (an example of such an XYZ file). The supercells were divided into stacks of 0.2-nm thick slices for the multislice calculation of the interaction of the electron wave with the sample. The multislice iteration and the electron optical imaging were calculated using the EMS image calculation software.[47] The parameters of the microscope were chosen for an LaB_6 electron gun filament, an equivalent to the tungsten filament in the CM-120 which was used for the acquisition of most of the images in this work. An aperture was applied to cut off the signal beyond the Scherzer point resolution of the instrument of about 0.25 nm.

2.4. X-ray Diffraction. X-ray diffraction (XRD) patterns were recorded with a TTRAX III (Rigaku) theta−theta diffractometer. The diffractometer was equipped with a rotating Cu anode operating at 50 kV (200 mA) and with a scintillation detector. The measurements were carried out in a specular diffraction ($2\theta/\theta$ scan) mode. Peak positions of the Bragg reflections and phase identification were determined using the Jade 9 software (MDI).

3. Results and Discussion

3.1. The Effect of Reaction (PLA) Temperature and Flow Rate. Scanning electron microscopy (SEM) images show clusters of quasi-spherical NP (Figure 3a). A close inspection (Figure 3b) shows a difference in contrast between the center and edges of the nanoparticles, indicating a hollow core. Figure 4a presents a transmission electron microscopy (TEM) image of NP clusters similar in size and shape to those seen in the SEM (Figure 3a). The obvious difference in contrast between the center and edges, is due to the hollow core. The NP were tilted by rotating the TEM grid to verify their shape and lighter contrast in the center and their chemical composition was verified by energy dispersive spectrometry (EDS) to be V_2O_5. A close-up (Figure 4b) shows that the hollow, quasi-spherical NP's are in fact crystalline and consequently can be considered as nearly perfect IF-V_2O_5 (NIF-V_2O_5).

---

(39) Enyashin, A. N.; Ivanovskaya, V. V.; Makurin, Y. N.; Ivanovskii, A. L. *Phys. Lett. A* **2004**, *326*, 152–156.

(40) Lakshmi, B. B.; Patrissi, C. J.; Martin, C. R. *Chem. Mater.* **1997**, *9*, 2544–2550.

(41) Hacohen, Y. R.; Popovitz-Biro, R.; Prior, Y.; Gemming, S.; Seifert, G.; Tenne, R. *Phys. Chem. Chem. Phys.* **2003**, *5*, 1644–1651.

(42) Parilla, P. A.; Dillon, A. C.; Jones, K. M.; Riker, G.; Schulz, D. L.; Ginley, D. S.; Heben, M. J. *Nature* **1999**, *397*, 114–114.

(43) Russo, R. E.; Mao, X.; Mao, S. S. *Anal. Chem.* **2002**, *74*, 70–77.

(44) Russo, R. E. *Appl. Spectrosc.* **1995**, *49*, 14A–28A.

(45) Chakrabarti, A.; Hermann, K.; Druzinic, R.; Witko, M.; Wagner, F.; Petersen, M. *Phys. Rev. B* **1999**, *59*, 10583–10590.

(46) Parker, J. C.; Lam, D. J.; Xu, Y. N.; Ching, W. Y. *Phys. Rev. B* **1990**, *42*, 5289–5293.

(47) Stadelmann, P. A. *Ultramicroscopy* **1987**, *21*, 131–145.

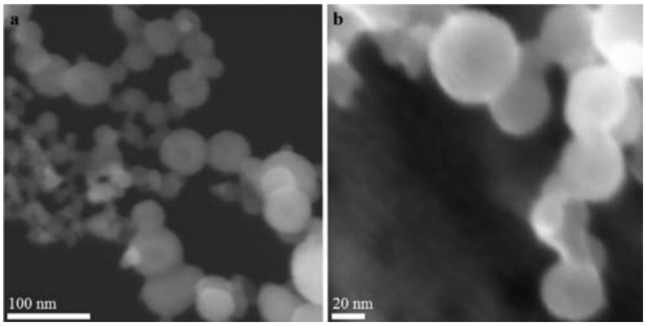

Figure 3. Scanning electron microscopy (SEM) images of (a) clusters of NIF-V_2O_5 NP obtained at a furnace temperature of 300 °C and a flow rate of 100 $cm^3 \cdot min^{-1}$ O_2.; and (b) close-up of NIF-V_2O_5 NP.

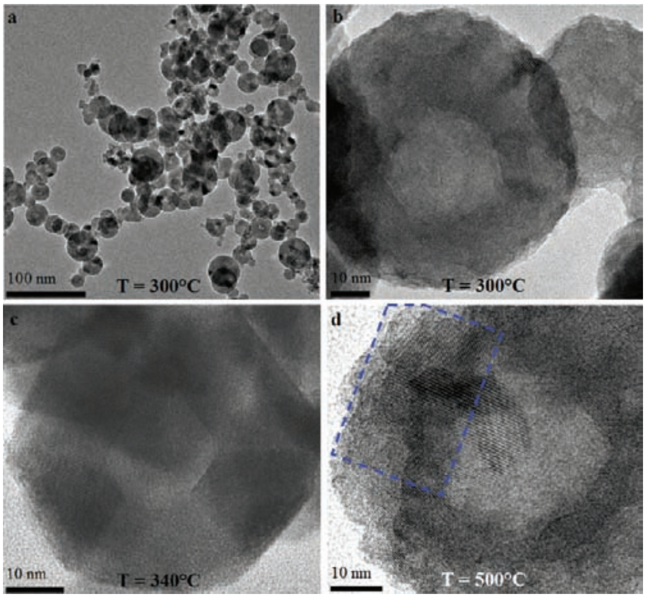

Figure 4. Transmission electron microscopy (TEM) images of PLA products obtained at a flow rate of 100 $cm^3 \cdot min^{-1}$ O_2 and a temperature of (a) 300 °C. (b) Close-up of an NIF-V_2O_5 NP. (c) 340 °C. (d) 500 °C. The blue dashed outline marks an elongated facet.

Of note is the fact that, while the outer surface appears quite spherical in shape and somewhat rugged, the contour of the inner surface of the NP is quite faceted. The wavy outlook of the outer surface is indicative of a surface reaction, possibly passivation by the ambient moisture. Contrarily, the straight appearance of the inner surface contours suggests that the reactivity of the closed NP has been substantially mitigated. Similar effects have been found in other closed-cage nanoparticles, most particularly with IF-Cs_2O NP.[10]

These NIF-V_2O_5 NP are observed as the temperature in the furnace (e in Figure 2) is increased to 300 °C and above and exhibit diameters ranging between 30 to 80 nm (Figures 3 and 4). Compact (nonhollow) V_2O_5 NP are observed between 50 to 500 °C as well. In fact the TEM analyzed product of experiments performed at 300 °C (Figures 3 and 4a,b) consisted of ∼60% NIF-V_2O_5 the rest being mainly compact spherical nanoparticles having a typical size of 10−80 nm. The product profile was similar at various sampling locations along the quartz tube.

At lower temperatures (50 °C) only small, compact NP (∼10−20 nm) are observed. Several nanoparticles with hollow cores, formed by the assembly and rearrangement of compact NP, were observed as well. These hollow nanoparticles are polycrystalline and distinctly different from the NIF-V_2O_5 which appear at 300 °C and above (Figure 4a,b). When the temperature is further increased, the NIF-V_2O_5 NP become more faceted (Figure 4c). Furthermore, NIF-V_2O_5 NP with elongated facets are clearly observed (blue outline in Figure 4d). A sharp increase in this trend is observed at 340 °C (Figure 4c). In addition, above 340 °C, V_2O_5 nanoplatelets and nanoneedles appear, while the yield of the NIF-V_2O_5 NP gradually diminishes with temperature (Supporting Information). The NIF-V_2O_5 produced at 300−350 °C were composed predominantly of α-V_2O_5 with no other discernible phases (see Supporting Information for X-ray and electron diffraction). The NIF-V_2O_5 size was also shown to increase with the furnace temperature and slightly decrease with the oxygen gas flow rate.

The aforementioned observations can be attributed to rapid annealing and crystal growth during the recoil of the plume into the furnace (e in Figure 2). The effect of postdeposition annealing of V_2O_5 films and the appearance of nanoneedles was reported in the literature.[15,48] Annealing of V_2O_5 nanoparticles in a carrier gas was previously reported,[36] and coarsening of the nanoparticles by sintering was observed.

A prominent feature is the extensive faceting of the NIF-V_2O_5 (Figure 4b). This is most probably due to the highly ionic character of the V_2O_5 2-D layered structure[7] which is much stiffer than the covalent WS_2 structure. The stiffer the bonds are, the harder it is to produce even bending, and new stress-relief mechanisms must be invoked.[41] For example, seams between straight α-V_2O_5 facets may be created by twisting the α-V_2O_5 lattice planes to create short γ-V_2O_5 segments (Figure 1a,b). Thus, bending into quasi-spherical structures is allowed by interlacing short γ-V_2O_5 segments between α-V_2O_5 facets. This would be in agreement with the sharp increase in faceting of the NIF-V_2O_5 NP at the γ to α transition temperature of 340 °C[22] (see section 2.2 for additional discussion).

The size of the NIF-V_2O_5 NP may be also tuned by the PLA conditions. In analogy to a related literature report,[49] the size of the NIF-V_2O_5 NP decreases with the increase of the carrier gas flow rate (f in Figure 2). This observation suggests that the coarsening of the NP is obtained also by attachment of moieties from the vapor phase onto the outer surface of the NP.

Ramana et al.[48] reported an exponential dependence of the domain size on the temperature during pulsed laser deposition of V_2O_5. Based on the above reports, the activation energy for domain growth in V_2O_5 was estimated to be 0.1 eV. This value indicates a kinetically controlled crystal growth process, as opposed to crystal growth controlled by diffusion of atoms through the solid. One then may assume that the domain growth activation energy[48] is similar to the crystal growth of the free-standing nanoparticles obtained by PLA in the present study. With this rational, and by taking an Arrhenius-like relation for the reaction rate constant, the NIF-V_2O_5 size at 500 °C is estimated (Supporting Information). Indeed, the calculated size of the NIF at 500 °C (70 nm) matches the experimental increase in NIF-V_2O_5 from 300 to 500 °C (∼40 nm to ∼70 nm) with a deviation of ±15% (see Supporting Information for a detailed explanation). Given the estimations made for the activation energy, the match between the observed and estimated sizes (based on the findings in[48]) is quite good. Therefore, it is plausible that the growth of the nanoparticles is partially

---

(48) Ramana, C. V.; Smith, R. J.; Hussain, O. M.; Julien, C. M. *Mater. Sci. Eng., B* **2004**, *111*, 218–225.

(49) Bi, X.; Kambe, N.; Kumar, S.; Gardner, J. T. In US Patent 7,214,446; NanoGram Corporation (Fremont, CA): United States, 2007.

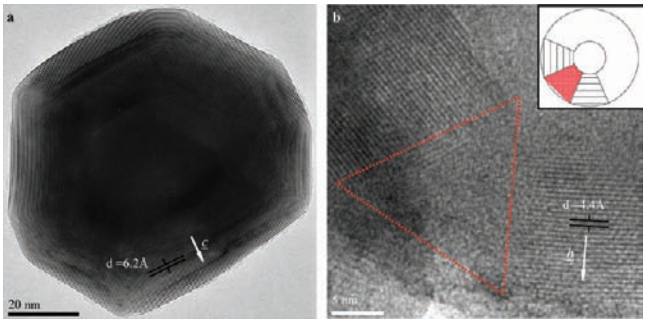

Figure 5. TEM images of (a) typical IF-WS_2 NP; (b) close-up of the lower left corner of the NIF-V_2O_5 in Figure 4b shows a wedge (red dashed triangle). (Inset) Wedge schematics marked by the full red triangle. The marked spacing between the concentric fringes is consistent with the vdW gaps of WS_2 and V_2O_5 ($\underline{c}$ and $\underline{b}$, respectively).

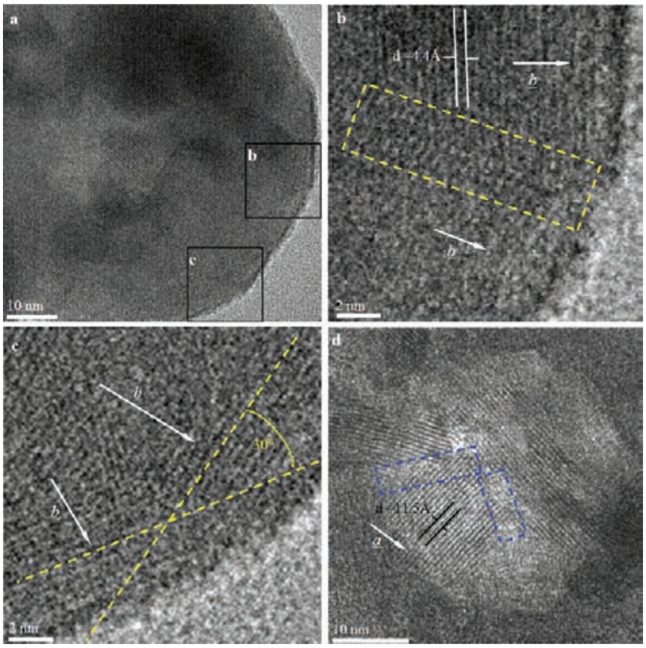

Figure 6. TEM images of (a) faceted NIF-V_2O_5, (b) close-up of concentric fringes, (c) intergrain boundary angle, (d) high-resolution TEM (HRTEM) image exhibiting intersections of radial fringes in the interior of an NIF-V_2O_5 outlined by the blue box.

controlled by the kinetics of the gas phase and surface diffusion of physisorbed moieties.

3.2. The Structure of NIF-V_2O_5 and the Formation Mechanism. The inorganic fullerene-like (IF) closed-cage structure is typically imaged in the TEM as made of concentric layers nested within each other, as in the case of IF-WS_2 (Figure 5a). The nested layers are parallel to the outer surface, with the vdW distance separating them (6.2 Å). Since $\underline{a} = \underline{b}$ the black quasi-circular fringes, which are produced by the scattering of the electron beam from the WS_2 molecular layers, look (almost) continuous and isotropic regardless of the viewing direction (Figure 5a). In the case of the MoS_2 nanooctahedra, pairs of triangular facets seam into edges and four edges coalesce into a rhombi.[5,6]

NIF-V_2O_5 nanoparticles exhibit similar concentric layers but with some additional disorder at the seams between the facets. The 4.4 Å spacing matches the $\underline{b}$ spacing which is the vdW gap (Figures 6b and 7b). While the NIF-V_2O_5 NP look similar to perfect inorganic fullerene-like structures, amorphous-looking wedges were observed between crystalline facets in all the reaction conditions tested (Figure 5b). However, a detailed examination of these wedges by tilting the NIF-V_2O_5 NP within the TEM revealed previously unseen facets which were probably out of the zone axis of the original viewing direction, thus appearing amorphous. It can be concluded therefore that the NIF-V_2O_5 NP are fully crystalline.

The NIF-V_2O_5 exhibit more complex characteristic features than their IF-WS_2 counterparts. The typical NIF-V_2O_5 NP produced at 300 °C possesses a quasi-spherical outline at its outer surface (Figures 3 and 4a,b) with numerous facets in a single NP (Figures 4b and 6b,c). Furthermore, radial fringes with a spacing of 11.5 Å are observed, consistent with the $\underline{a}$ spacing (Figure 6d). These radial fringes create apparent grain boundaries with each other (Figure 6d). The appearance of the radial fringes suggests a commensuration between the layers of the inspected domain. This observation is nontrivial, since the number of atoms in the layers increases with increasing radial position from the center of the nanoparticle. The commensuration between the layers in a given domain indicates that the V_2O_5 layers in each rectangular facet are terminated by defects which stitch the domains into a multifaceted closed structure. This closure mechanism is very different from the one found in e.g. IF-WS_2 where the layers are continuous, (almost) defect free and incommensurate with respect to the upper and lower molecular layers of the closed NP (Figure 5a).

The electron irradiation sensitivity of the NIF-V_2O_5 results in rapid beam damage when imaged in the electron microscope. This beam-induced damage imposes severe restrictions on the TEM analysis, allowing taking only a few images for each nanoparticle. Complementary information on the structure of the NIF-V_2O_5 NP may be gained by model calculations of the TEM imaging. This is accomplished by first constructing a structural model which can be fitted to partial sections of the NIF-V_2O_5.

The model stipulates that the rectangular bulk symmetry of the V_2O_5 orthorhombic lattice is preserved with the $\underline{b}$ axis pointing outward in the hollow, closed nanoparticles. Additionally, special attention to the seaming of the facets is required. The facets should be seamed such that their orientation with respect to the neighboring facets avoids forcing a connection of two oxygen (vanadium)-terminated edges to each other, for example. Finally, the plane projection of the structure must possess a multifaceted appearance, in agreement with the general features revealed by the TEM images (Figure 6b,c). The nested layers of this structure should be fully commensurate in agreement with the observed radial fringes (Figure 6d).

The above requirements highlight the difficulty in constructing a complete single model of the NIF-V_2O_5. Moreover, limited computational resources impose constraints on the size of the modeled nanoparticles, forcing one to use significantly smaller structures than those observed in the experiment. These considerations also place a constraint on the number of grain boundaries tested as opposed to the large variety of possibilities. Thus, a simplified partial model will be presented, in order to explain the experimental findings.

A rather simplified model consisting of a single V_2O_5 layer is constructed with square facets each composed of a single 2-D V_2O_5 (010) layer fragment and 8 triangles in a rhombicubooctahedron arrangement (Figure 7a). A molecular detail of a portion of such a model is presented in Figure 7b. The facets are seamed together at a tangent of 45° (marked by the dashed line in Figure 7b). This angle is obviously quite different from the experimentally observed angle (30°) between the

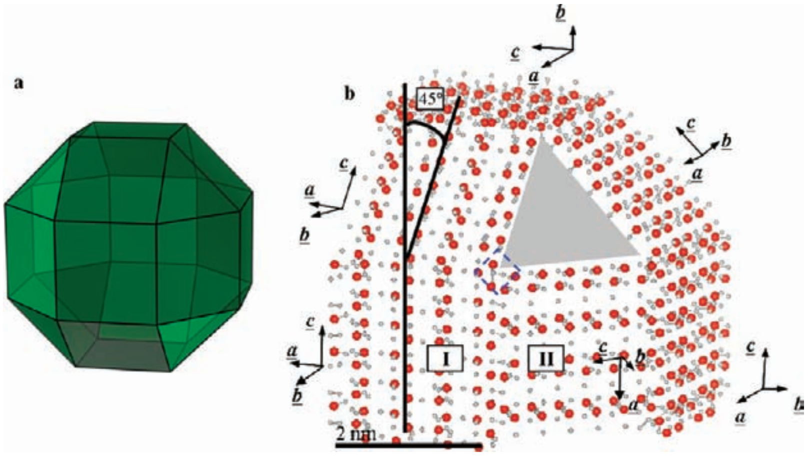

Figure 7. Simplified model of an NIF-V_2O_5. (a) Scheme of a rhombicubooctahedron. (b) Section created by the fragments of a single 2-D V_2O_5 layer seamed at an angle of 45° which is the intergrain boundary angle used in the model (marked by the black line). The gray triangle highlights a triangular facet which is not modeled. Each set of axis describes the closest facet. (I) and (II) describe adjacent facets that are rotated by 90° with respect to each other. The blue line highlights an intersection point of four facets.

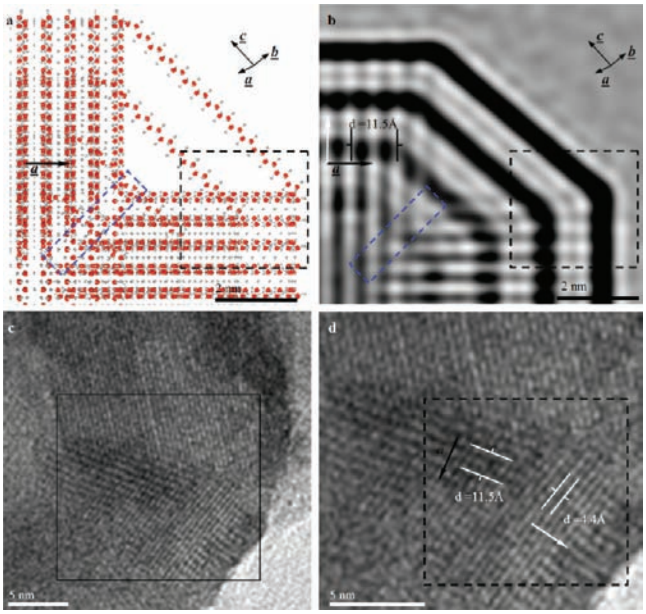

Figure 8. (a) Series of stacked sections created by four V_2O_5 layers. (b) Simulated TEM image of (a). The defocus in the image is −15 nm (underfocus). Blue lines highlight an apparent grain boundary created by a series of four individual intersection points such as the one seen in Figure 7b. Crystal directions describe the upper right facet. The spacing between the sections (vdW gap) is not to scale, being 13.9 Å instead of the experimental value of 4.4 Å. (c) Section of an NIF-V_2O_5 from Figure 4b. (d) Close-up of (c). The black lines in (b−d) highlight the observed overlap of the radial and concentric fringes marked by the white arrows designated $\underline{a}$ and $\underline{c}$, respectively. The radial fringes are marked by the black arrows, and the concentric fringes are marked by the white arrows.

domains as shown in Figure 6c. The selection of the 45° angle was dictated by the simplified nature of the model. Furthermore, the interlayer distance ($\underline{b}$) between the V_2O_5 layers (13.9 Å) is appreciably larger than the vdW gap (4.4 Å). This distance is dictated by the need to fulfill the commensuration condition between the layers. A quasi-spherical section requires seaming of facets that are rotated by 90° with respect to each other (I and II in Figure 7b). Similar models with larger facets are then added to create a simplified model of an NIF-V_2O_5 section with four layers (Figure 8a). Further comparison of the simplified model with the experimental images was performed by TEM image simulation using the EMS program[47] (Figure 8b).

The seams between facets (edges and apexes) are likely to be composed of defective domains which unfortunately could not be considered in the construction of the model. As a result, this model has a triangular facet which cannot be adequately modeled (marked by the gray triangle in Figure 7b). This is due to the orthorhombic crystal structure of V_2O_5 which does not allow construction of perfectly crystalline triangular facets (cut along the (3 0 1) plane) with perfect seaming to the neighboring rectangular (0 1 0) facets. While a quasi-triangular facet can be built stepwise, the edge atoms would invariably possess dangling bonds. Thus, seaming the stepwise triangular facet to neighboring facets would require the use of defective domains at the edges and apexes.

The model explains why no completely concentric fringes are observed in the TEM images as opposed to IF-WS_2. In the latter example the lattice vectors $\underline{a} = \underline{b}$[3], which results in identical seams between facets. Thus, the 2-D layers look identical regardless of the viewing direction. Here a significantly more complex structure is being closed up with radically different unit cell dimensions ($\underline{a} \approx 3.2\underline{c}$) forcing it into forming a less symmetric NIF nanoparticle.

The TEM image simulation of the model displays several features seen in the experimental images, the most obvious being the radial fringes with the 11.5 Å spacing (marked by the black arrow in b and d of Figure 8, respectively). These fringes seem to overlap the concentric fringes (marked by the white arrow in b and d of Figure 8). Furthermore, an apparent grain boundary highlighted by the blue line in the TEM image simulation (Figure 8b) is experimentally observed (Figure 6d). In the three-dimensional space, the nested cages produce what appears to be a grain boundary. This effect is created by tracing out the intersection point of four facets (the blue box in Figure 7b) as additional sections are added. Furthermore, the amorphous looking wedges may be attributed to the triangular facets. Therefore, the model may be used to investigate various structural aspects of the NIF-V_2O_5 nanoparticles, most particularly the evolution of the facet structures during annealing (*vide infra*).

The NIF-V_2O_5 structure may be understood better in light of their most plausible formation mechanism. It is believed that initially, liquid nanodroplets of V_2O_5 form (mp = 680 °C[24]) in the recoiling plume (d in Figure 2). These nanodroplets undergo

Table 1. Bulk Properties and Respective Nanostructures of Various Materials

material	bond ionicity (%)	structure (no. of atoms in unit cell)	closed-cage NP shape	seaming
WS_2	1	*P6₃/mmc*; 2H-MoS_2 (6)	quasi-spherical; faceted	quite perfect
MoS_2	4	*P6₃/mmc*; 2H-MoS_2 (6)	IF - quasi-spherical; faceted	quite perfect
			nanooctahedra; very faceted	perfect
$NiCl_2$	32	*R3m*; 3R-$CdCl_2$ (9)	quasi-spherical (2 layers)	quite perfect
			very faceted (>3 layers)	
$CdCl_2$	42	*R3m*; 3R-$CdCl_2$ (9)	hexagonal outline; highly faceted	quite perfect
V_2O_5	55	*Pmnm* (14)	quasi-spherical (furnace temperature of up to 300 °C); highly faceted	imperfect
			5−8-sided outlines (340 °C and above); highly faceted	quite imperfect (small amounts)

rapid quenching to form compact amorphous V_2O_5 NP. Finally crystallization from the surface inward takes place (possibly in the furnace in Figure 2d). This step leaves a hollow core, since the crystalline phase[50] is denser than the amorphous phase as described by Hevesi,[51] Livage,[52] and their co-workers. The solidification of the molten droplets into amorphous (full) NP is inferred from the quasi-spherical shape (Figures 3 and 4a,b) of the NIF-V_2O_5 NP. This is further supported by the V_2O_5 melting point (680 °C[24]) as compared to the plume temperature which can reach temperatures of up to 2000 °C.[41] A rapid quenching process of liquid nanodroplets is likely to create quasi-spherical, amorphous V_2O_5 NP.[25]

Furthermore, an inspection of the ratio of the inner to outer radii of the NIF-V_2O_5 reveals a consistent value of 1:2.5 to 1:3. Equation 1 shows that such a ratio would require a 4−6% density increase from the initial (full NP) to the final crystalline V_2O_5 state (hollow nanoparticles). The required density of the initial state is closely matched by amorphous V_2O_5 (7−11% density increase[51,52]) as opposed to liquid V_2O_5 (30%[24]). It is therefore believed that the formation mechanism of the NIF-V_2O_5 is induced by a crystallization of amorphous V_2O_5 NP, whose size primarily determines the size of the NIF-V_2O_5 nanoparticles.

$$\frac{\rho_{\text{initial}}}{\rho_{\text{final}}} = \frac{V_{\text{total}} - V_{\text{inner}}}{V_{\text{total}}} = 1 - \left(\frac{r_{\text{inner}}}{R_{\text{outer}}}\right)^3; \quad \frac{R}{r} = 2.5 - 3 \Rightarrow \frac{\rho_{\text{initial}}}{\rho_{\text{final}}} = 0.94 - 0.96 \qquad (1)$$

In general the crystallization starts at various loci on the amorphous NP surface. The lateral propagation of the crystalline domains may lead to lattice mismatch, thus giving rise to defects at their grain boundaries. Moreover, this process would account for several observed features of NIF-V_2O_5, such as the highly faceted inner surface[53] and the sharp angles between the facets (Figures 4b and 6d). These features form as the crystallization front nears the inner surface which has an increased radius of curvature, thus decreasing the number of facets that form. A similar effect is observed during the inward crystallization of IF-WS_2.[3]

The proposed growth mechanism could account also for the formation of the small (∼15 nm) and crystalline NP observed at 50 °C. It is believed that due to insufficient annealing the seaming between the domains was incomplete. In fact, hollow nanoparticles (∼35 nm) made of imperfectly seamed nanoparticles (∼10 nm) are occasionally observed at 50 °C.

Occasionally, NP's with off-center hollow core are seen (Figure 4b). This observation suggests that the crystallization of one or more domains is retarded with respect to the others. Furthermore, an uneven spatial and temporal spread of crystallization locations would result in an asymmetric distribution of the facets (Figure 4b,c). A sufficiently large time difference may even result in fully compact NP.

The coalescence of the domains' growth fronts implies the formation of structural defects. One possible defect may be γ-V_2O_5 segments interlaced between the α-V_2O_5 facets thus allowing bending into quasi-spherical shapes. This hypothesis would be in agreement with the sharp increase in faceting when the NP are annealed at 340 °C which is the γ to α transition temperature[22] (Figure 4c).

Topologically, a concave polyhedron cannot be constructed with rectangular facets alone. Therefore, some of the growing rectangular facets will inevitably converge at nonright angles when forming an edge or apex. This may result in the formation of quasi-triangular facets as indicated by the simplified model (Figure 7b). However, as noted above such triangular facets cannot be perfectly seamed to the neighboring rectangular polygon, giving rise to defects.

The upper (∼100 nm) and lower (∼30 nm) limits of the NIF-V_2O_5 size may be related to their structure. The main driving force for the formation of closed-cage structures from layered bulk materials is related to the exposure of the low-energy surface (the vdW surface) outward to the ambient.[53] This energetic gain must compensate for the stress energy inherent in the closed-cage structure. In IF-WS_2 NP for example, this stress is relieved by bending of the rather flexible layers, which entails lack of full commensuration between the adjacent layers and some faceting.[3]

In the case of the NIF-V_2O_5 NP the bending option is not available due to the increased ionic character of the V_2O_5 bonds. This leaves faceting as the main stress-relief mechanism in the closed-cage NIF-V_2O_5 NP. As the diameter of the NP become smaller toward the core the number of facets is reduced and the angles between the facets become sharper with a higher energetic cost due to the increase in the radius of curvature. On the other hand, at larger diameters the driving force for the NIF-V_2O_5 formation due to the edge effect, i.e. the rim atoms with unsaturated bonds, becomes negligible when compared to the bulk volume. Consequently, the stress release mechanism by faceting places inherent upper and lower limits on the NIF-V_2O_5 size.

Further insight into the formation of hollow nanoparticles of layered (2-D) compounds can be inferred from the following sequence (see Table 1). Preliminary discussion of these ideas

---

(50) Liu, Z.; Fang, G.; Wang, Y.; Bai, Y.; Yao, K. L. *J. Phys. D: Appl. Phys.* **2000**, *33*, 2327–2332.

(51) Michailovits, L.; Bali, K.; Szorenyi, T.; Hevesi, I. *Acta Phys. Acad. Sci. Hung.* **1980**, *49*, 217–221.

(52) Mosset, A.; Lecante, P.; Galy, J.; Livage, J. *Philos. Mag., Part B* **1982**, *46*, 137–149.

(53) Feldman, Y.; Frey, G. L.; Homyonfer, M.; Lyakhovitskaya, V.; Margulis, L.; Cohen, H.; Hodes, G.; Hutchison, J. L.; Tenne, R. *J. Am. Chem. Soc.* **1996**, *118*, 5362–5367.

was presented in ref 41. One may consider the following series of molecules with 2-D structure: WS_2 (MoS_2), $NiCl_2$ ($CdCl_2$), and V_2O_5. Some insight into the formation of hollow, closed nanoparticles may be gained by comparing their Pauling's bond ionicity,[54] lattice structure, and the complexity of the unit cell (number of atoms).

The increase in ionicity results in increased faceting of the closed-cage NP shape due to increased stiffness of the lattice. The asymmetry in the 2-D crystal structure of the layer and the complexity of the unit cell renders the seaming of the facets increasingly difficult, resulting in imperfect seaming. Vanadium pentoxide, being the extreme point of reference in both of these trends, showcases the issue of stiffness and seaming. Thus, a generalization for which layered materials can form genuine closed-cage structures can be made. The formation of such nanostructures would be favored in layered materials with low ionicity and simple and symmetric (i.e., $a = b$) unit cells, such as various transition metal dichalcogenides.

4. Conclusions

In conclusion, hollow, closed nanoparticles of V_2O_5, which are closely associated with the fullerene-like (IF) nanoparticles of WS_2 (MoS_2) were produced by pulsed laser ablation. It is believed that the amounts of the NIF-V_2O_5 products may be scaled up by other methods such as spraying molten V_2O_5. The growth mechanism and the structure of these nanoparticles were characterized by a variety of techniques and via structural modeling. It was concluded that the nearly perfect NIF-V_2O_5 nanoparticles are entirely crystalline and are made patch-wise with their low-energy surface (010) pointing outward with some defects between the facets. The generality of the mechanism indicates that new IF and INT are expected to be obtained by the crystallization of amorphous nanostructures with a layered crystal structure, such as the transition of amorphous MoS_3 to 2H-MoS_2 nanoparticles. The results of this work and previous results were used to formulate a guideline as to which layered materials are favored for the formation of IF and INT.

Acknowledgment. We thank Mark Schneider for his assistance in the SEM imaging, Dr. Yishay Feldman for the XRD, and Dr. Rita Rosentzveig for the assistance with the gas flow system. This work was supported by the ERC Grant INTIF 226639, the Israel Science Foundation, the Irving and Cherna Moskowitz Center for Nano and Bio-Nano imaging, and the Harold Perlman Foundation. R.T. holds the Drake Family Chair in Nanotechnology and is the director of the Helen and Martin Kimmel Center for Nanoscale Science.

Supporting Information Available: Sizes and the morphologies of NIF-V_2O_5 obtained at various conditions: Table S1; details and summary of comparison between theoretical and experimental NIF-V_2O_5 sizes at 500 °C: Table S2; XYZ file containing the atomic co-ordinates of a single-shell V_2O_5 nanoparticle model. This material is available free of charge via the Internet at http://pubs.acs.org.

JA103719X

---

(54) Garcia, A.; Cohen, M. L. *Phys. Rev. B* **1993**, *47*, 4215.

(55) Teller, R. G.; Antonio, M. R.; Brazdil, J. F.; Grasselli, R. K. *J. Solid State Chem.* **1986**, *64*, 249–260.